Solar Energy 298 (2025) 113743

Contents lists available at ScienceDirect

Solar Energy

journal homepage: www.elsevier.com/locate/solener

Comparison of the corrosion of ferritic and austenitic stainless steel (AISI 430 and AISI 316L) with LiNaK carbonate salts for thermal energy storage in CSP/CST applications

Mafalda Gil [*], Fátima Pedrosa, Teresa Paiva, Isabel Figueira, Fernando A. Costa Oliveira, Teresa C. Diamantino

Laboratório Nacional de Energia e Geologia I.P. (LNEG), Estrada do Paço do Lumiar, 22, 1649-038 Lisboa, Portugal

ARTICLE INFO

Keywords:
Corrosion
Thermal energy storage
LiNaK carbonate salts
Molten salts
Stainless steels
Concentrated solar thermal

ABSTRACT

This study focuses on the corrosion rates and mechanisms of two stainless steels, austenitic AISI 316L and ferritic AISI 430, in contact with a eutectic mixture of LiNaK carbonates in long-term tests at 650 °C. The selection of these two stainless steels was based on their differences, both in their intrinsic characteristics and in the cost associated with each one. The research also underscores the importance of optimizing the descaling methods used to evaluate the corrosion rate. Corrosion rates were measured gravimetrically according to ISO 17245:2015, revealing an asymptotic behavior for both steels, with AISI 430 with a corrosion rate of 237 ± 21 μm and AISI 316L of 151 ± 13 μm after 2000 h of testing. Corrosion mechanisms were analyzed using SEM/EDS, GDOES, and XRD techniques, which identified well-defined oxide layers with varying compositions. Given the observed corrosion mechanisms and its lower cost, AISI 430 steel seems to have great applicability in CSP/CST plants, provided it is paired with an appropriate protective coating.

1. Introduction

The demand for clean, safe, and sustainable energy has become a global necessity. In this context, renewable energy sources are being utilized more frequently. Photovoltaic systems and wind turbines are two common technologies that convert solar and wind energy into electricity for various applications, including residential use, greenhouse buildings, agriculture, and water desalination. However, these renewable energy sources are variable, leading to significant intermittent and fluctuations in power generation. Researchers are exploring the viability of adding energy storage systems to power plants to address existing challenges. Concentrated solar power (CSP) or concentrated solar thermal (CST) technology shows great promise for generating electricity from solar energy. CSP/CST plants are particularly effective because they can store large amounts of thermal energy collected during the day using thermal energy storage (TES). This capability allows the plants to release stored energy at night, providing power on demand and giving CSP/CST plants an economic advantage over other renewable energy technologies. Notably, this improvement in electric power generation can increase output by up to 25 % [1,2]. CSP systems function based on a straightforward principle. Mirrors focus solar radiation onto a receiver, where the heat is absorbed and transferred to a specific fluid called the heat transfer fluid (HTF) [3,4].

Solar Salt is the most commonly used TES material in CSP systems. It is a eutectic mixture consisting of 60 % sodium nitrate ($NaNO_3$) and 40 % potassium nitrate (KNO_3) by weight. Its popularity stems from its low cost, good chemical safety (as it is non-toxic and non-flammable), and reasonable material compatibility, which allows the use of common stainless steels without incurring high corrosion rates. However, the operating temperature range is constrained by a crystallization temperature of approximately 240 °C and a maximum operating temperature of around 565 °C. Beyond this temperature, the salt begins to decompose, leading to its degradation [5].

To enhance the efficiency of energy conversion into electricity, it is essential to establish a temperature range of up to 600 °C. Achieving this necessitates the development of new mixtures of molten salts, incorporating either fluorine or chlorine, or using carbonates that can function at elevated temperatures.

Lithium plays a crucial role in molten salt formulations due to its unique properties, which make it particularly suitable for storage

---

[*] Corresponding author.
E-mail address: mafalda.gil@lneg.pt (M. Gil).

https://doi.org/10.1016/j.solener.2025.113743
Received 18 February 2025; Received in revised form 27 May 2025; Accepted 27 June 2025

Table 1
Corrosion rates (μm/year) of stainless steels immersed in LiNaK carbonate salt from literature.

Steel (AISI)	Molten salt composition (wt. %)	Temperature (°C)	Test time (h)	Corrosion rate evaluation methodology	Corrosion rate (μm/year)	Ref
316L	Na_2CO_3-Li_2CO_3-K_2CO_3 (35.3–10.2–54.5)	600	1440	Descaling method according to ASTM G1–03 C.7.5	400	[15]
	Na_2CO_3-Li_2CO_3-K_2CO_3 (31.2–15.5–53.3)				320	
	Na_2CO_3-Li_2CO_3-K_2CO_3 (38–33-29)				220	
316	Na_2CO_3-Li_2CO_3-K_2CO_3 (33.4–32.1–34.5)	700	168	Descaling method according to ASTM-G1-03 (5.55 wt% HCl)	121	[16]
			336		12	
			504		$\Delta m \leq 0$	
P91	Na_2CO_3-Li_2CO_3-K_2CO_3 (33-32-35)	650	1000	Without information	2686	[17]
310	Na_2CO_3-Li_2CO_3-K_2CO_3 (33.4-32.1-34.5)	600	600	Without information	390	[18]
310S	Na_2CO_3-Li_2CO_3-K_2CO_3 (32-43-25)	650	600	Descaling method according to ISO 17245 C.7.10	100	[19]
301LN	Na_2CO_3-Li_2CO_3-K_2CO_3 (33.4-32.1-34.5)	600	1000	Descaling method according to ASTM-G1-03 (10 % HCl) and cross-sectional analysis for oxide scale thickness	320 ± 90 (corrosion rate is identical when using either method)	[20]
2205	Na_2CO_3-Li_2CO_3-K_2CO_3 (33–32-35)	600	1000	Loss of thickness	510 ± 90	[21]

applications. It contributes to an increase in heat capacity and energy density in both electrical and thermal systems [6].

Lithium-based carbonate salts are regarded as the most promising option for use in CSP plants. This study focuses on a eutectic mixture consisting of 32 wt% Li_2CO_3, 33 wt% Na_2CO_3, and 35 wt% K_2CO_3, which exhibits excellent thermophysical properties. These include a density of 2.09 g/cm^3 (at 397 °C), a latent heat of fusion of 276 J/g, thermal conductivity of 0.612 W/(m.K) at 757 °C, and a heat capacity of ~1.6 J/(g. K) [6–8]. Furthermore, it exhibits elevated thermal stability, with decomposition temperatures of 1000 °C, 700 °C and 670 °C in an atmosphere of carbon dioxide, argon and air, respectively [8].

These salts present challenges due to their corrosive effects on structural materials [6]. In TES systems, the materials used for pipes, valves, and pumping components vary based on the operating temperature, and they can be susceptible to severe corrosion. Carbon steel is recommended for temperatures below 300 °C, stainless steel for temperatures ranging from 300 °C to 550 °C, and Ni-based alloys are mandatory for operating temperatures above 550 °C [2].

Choosing the structural material to be used in a CSP plant requires careful consideration, as the decision should prioritize economic advantages. Several factors influence this choice, including cost, the plantś expected lifespan, resistance to corrosion, operating temperatures, and the type of heat transfer fluids used. Each of these elements plays a critical role in determining the most suitable material for the plant.

Studying the compatibility of structural materials with molten salts is crucial, particularly regarding their corrosiveness. The chemical composition and structural characteristics of materials determine their behavior in contact with molten salts. The presence of certain elements, such as chromium and nickel, has been demonstrated to increase corrosion resistance, as they have a positive impact as a barrier against further oxidation. The presence of chromium facilitates the formation of a protective oxide layer; however, the presence of nickel enhances the stability of the oxide formed [9,10].

While nitrate mixtures have been extensively studied for corrosion with various materials [2,11–14], the corrosiveness of carbonate salt mixtures is still relatively underexplored. Moreover, understanding the corrosion mechanisms is essential for gaining insights into how structural materials behave when exposed to high temperatures and in contact with carbonate salts, especially the mixtures of lithium, sodium and potassium.

Table 1 presents the corrosion rate values of stainless steels with carbonate salt mixtures, as reported in the literature under various testing conditions.

Gallardo-González *et al.* [15] investigated the corrosion resistance of the austenitic AISI 316 stainless steel when exposed to various mixtures of Li_2CO_3-Na_2CO_3-K_2CO_3 for 1440 h at 600 °C. They found that the corrosion rate decreased as the amount of lithium carbonate in the molten salt mixture increased.

Liu *et al.* [16] studied the behavior of AISI 316 submerged in the carbonate salt LiNaK for 21 days at 700 °C. They observed a mass gain rather than a loss, which was unexpected. The authors suggest that this could be attributed to the formation of protective compact layers on the surface of the steel.

Audigié *et al.* [17] investigated the corrosion of the ferritic P91 stainless steel when immersed in a eutectic mixture of Li_2CO_3-Na_2CO_3-K_2CO_3 up to 1000 h at a temperature of 650 °C. This study revealed that this alloy exhibits poor corrosion resistance under these conditions.

When comparing the results for P91 [17] and AISI 316L [15] (see Table 1), it is evident that P91 has a higher corrosion rate than 316L steel, although the tests were conducted at a higher temperature for P91.

Morales *et al.* conducted two studies [20,21]. In the first study, they used AISI 301LN steel and found that employing two different methodologies for assessing corrosion rates did not affect the resulting values. In the second study, which involved duplex steel, they observed that this material exhibited a higher corrosion rate compared to austenitic steels.

Table 1 shows that Gallardo-González *et al.* [15], Liu *et al.* [16], Sah [19], and Morales *et al.* [20] applied chemical methods through descaling in accordance with two standards: ASTM-G1-03 and ISO 17245. However, neither Audigié *et al.* [17] nor González-Fernández *et al.* [18], did not specify which methodology they used to assess the corrosion rate. Additionally, Morales *et al.* [20,21] employed a methodology that involves measuring the loss of oxide thickness formed after corrosion tests.

It is also important to consider other variables that are not described in the table, such as the degree of purity of the salt and its respective impurities. These additional factors have been demonstrated to influence the results of corrosion tests [10]; however, they are often not addressed in literature [19]. Therefore, due to variations in results, test durations, temperatures and gradients, methodologies, salt purity and its impurities, comparing the corrosion rates obtained across these different studies is pretty challenging.

There are gaps in knowledge of new salts, such as carbonate salts, as well as the mechanism of corrosion involving ferritic steels. Additionally, there is a lack of standardized methodologies for measuring corrosion rates, particularly with regard to longer immersion times and various descaling methods. For this reason, this work aims to study the

Table 2
Elemental composition of AISI 430 and AISI 316L stainless steels.

Grade of steel (AISI)	Chemical composition (wt.%)											
	C	Mn	Si	P	S	Cr	Ni	Mo	N	Cu	Co	Fe
430	0.037	0.310	0.350	0.028	0.001	16.260	0.270	0.020	0.048	0.160	0.020	Bal.
316L	0.022	1.276	0.349	0.026	0.001	16.630	10.060	2.144	0.039	–	–	Bal.

Table 3
Impurities present in the LiNaK carbonates.

	As	Cl	Fe	Hg	Pb	SO_4^{2-}	Heavy metals	Na (%)
$Na_2CO_3^a$ (ppm)	1	0.25	30	1	1	300	–	–
$K_2CO_3^{(1)}$ (ppm)	3	48	0.22	0.05	2	41	5	0.21
$Li_2CO_3^{(2)}$	Elemental analysis detected Mg, As, Ca, S, P, Si							

(1) Certificate of analysis provided by the supplier.
(2) X-ray fluorescence analysis was performed since the supplier did not provide this information.

corrosion rates and mechanisms of two stainless steels, austenitic AISI 316L and ferritic AISI 430, in contact with a eutectic molten salt mixture of lithium, sodium and potassium carbonates, in long-term tests at 650 °C. The corrosion test temperature of 650 °C was selected based on the melting temperature (397 °C), the decomposition temperature of salt in air (670 °C) [8] and the limit for acceptable thermal degradation, which according to various authors, is when there is a weight loss of 3 % [22]. With regard to AISI 430 steel, no corrosion studies were found with this molten salt mixture and this steel is less expensive than austenitic steel. Additionally, the study emphasizes the importance of standardizing the methodologies used for corrosion testing, as well as the techniques employed to evaluate corrosion rates.

2. Experimental

2.1. Material samples

The choice of these two stainless steels was based on their differences, specifically in their inherent properties – austenitic steel *versus* ferritic steel – as well as the associated costs, with AISI 430 being more affordable than AISI 316L.

Rectangular samples measuring approximately 30 mm × 40 mm and 4 mm thick were machined from AISI 316L and AISI 430 steels sourced from Acerinox Europa and Acciai Speciali Terni, respectively. The elemental composition of the two stainless steels is presented in Table 2. Before conducting corrosion tests, the coupons were ground using 320-grit SiC abrasive paper on a grinding wheel. Following this, they were degreased with ethanol and rinsed with distilled water. Finally, the dimensions and weights of the coupons were recorded.

The corrosion tests utilized a ternary mixture of molten salts consisting of Li_2CO_3 (from Alfa Aesar), Na_2CO_3 (from Tata Chemicals Europe) and K_2CO_3 (from Armand Products Company). These salts had a purity of 99 % and were mixed in the following weight ratios: 32.1:33.4:34.5 m/m. Table 3 details the impurities present in each salt. Before the tests, the salts were dried in an oven at 110 °C for 24 h to remove any residual moisture.

2.2. Testing conditions

Corrosion tests on stainless steels were carried out in alumina crucibles within a muffle furnace at 650 °C. These tests lasted up to 2000 h and involved direct contact with a ternary mixture of molten salts composed of 32.1 % Li_2CO_3, 33.4 % Na_2CO_3 and 34.5 % K_2CO_3. The conditions were static and took place in an air atmosphere.

In these tests, four replicates were taken for each exposure time, 8 h, 24 h, 48 h, 72 h, 120 h, 240 h, 480 h, 1000 h, 1440 h, and 2000 h. After the specified exposure period, the specimens were removed from the crucibles and transferred to a beaker containing hot distilled water. This step was performed to remove any salts that may have adhered to the surface of the specimens. Once the washing and drying processes were complete, the specimens were weighed to calculate the mass gain. For the gravimetry (descaling process), three replicates were used, while the remaining replicate was subjected to surface and cross-sectional characterization using Scanning Electron Microscopy with Energy Dispersive X-ray Spectroscopy (SEM/EDS), Glow Discharge Optical Emission Spectrometry (GDOES) and X-ray Diffraction (XRD) analysis.

Table 4
Procedures for the three descaling methods outlined in the standards ISO 17245 [23] and ISO 8407 [24].

Method	Designation	Chemical agents	Time	Temperature
1	C.7.10 [23]	Step 1: 45 g of NaOH 7.5 g of $KMnO_4$ Distilled water to make 250 mL	40 min	Boiling
		Step 2: 25 g of $(NH_4)_2C_6H_6O_7$ Distilled water to complete 250 mL	40 min	Boiling
2	C.7.2 [24]	400 ml of HNO_3 (ρ = 1.42 g/mL) Distilled water to make 2000 mL	60 min	Heat until 60 °C
3	C.7.9 [24]	40 ml of HNO_3 (ρ = 1.42 g/mL) 8 ml of HF [ρ = 1.16 g/mL (47 % by mass fraction HF to 53 % by mass fraction HF)] Distilled water to make 400 ml	20 min	20 °C to 25 °C

Additionally, it was investigated whether polishing the surface of the samples AISI 430 affects the corrosion rate and optimizing the descaling method used for effectively removing the oxide layer formed on AISI 316L stainless steel when it comes in contact with the ternary carbonate salt.

Table 4 outlines the three descaling methods evaluated in this research. The first method follows ISO 17245:2015 [23], which is specifically designed for corrosion tests of heat-resistant stainless steels immersed in salts. The other two methods are tailored for steels according to ISO 8407:2021 [24].

The corrosion rate (CR) was determined, in terms of thickness per year, after descaling the corrosion products and based on the mass loss recorded according to:

$$CR(\mu m/yr) = \frac{87600\Delta m}{\rho t} \tag{1}$$

where Δm is the mass change per unit area after descaling (mg/cm^2); ρ is the density of the stainless steel: $\rho_{AISI\ 316L} = 7.98\ g/cm^3$, $\rho_{AISI\ 430} = 7.7\ g/cm^3$; t is the immersion time (h).

2.3. Characterization techniques

The Scanning Electron Microscope, Model Phillips XL 30 FEG, along with X-ray microanalysis, was utilized to assess the morphology and the semi-quantitative elemental chemical composition of the corrosion products, both in cross-section and on the surface. Images were captured utilizing secondary and backscattered electrons, with an energy of 15 keV applied. For the cross-sectional analysis, the test specimens were mounted in Polyfast resin, a conductive resin suitable for hot mounting. The samples were initially roughened with sandpaper of varying grit sizes (220, 320, 500, 800, 1000, 2500), followed by fine polishing with diamond pastes of 1, 3, and 6 µm.

To reveal the microstructure of the steels, the polished samples were etched with different contrast solutions before and after exposure to the carbonate salt (0 h and 2000 h). For the AISI 430 steel, Vilella's Reagent, consisting of 0.5 g acid picric, 50 mL ethanol and 2.5 mL HCl, was applied for 60 s. For the AISI 316L steel, Acetic Glyceregia made from 15 mL HCl, 10 mL HNO_3, 10 ml of acetic acid, and 2 drops glycerin, was used for 15 to 20 s.

The Glow Discharge Optical Emission Spectroscopy (GDOES) depth profile analysis of the oxides was carried out using a Horiba GD Profiler 2, which is equipped with a 4 mm diameter anode. The analysis was conducted under a typical radio frequency discharge pressure of 650 Pa and power setting of 30 W, in an argon atmosphere.

The structural characterization of the stainless steel samples after the corrosion tests was performed using X-ray diffraction analysis. The results were then compared to those of the initial steel samples (*i.e.* before the corrosion tests). A Bruker AXS D8 Advance diffractometer, which utilizes Cu Kα radiation, was employed for the analysis. The applied voltage was set at 40 kV, and the current was 40 mA. The diffraction patterns were analyzed using the Diffrac Measurement Centre V8 software from Bruker AXS. The crystalline phases were identified with the DIFRAC.EVA V6.0 software, utilizing the ICDD PDF-2 database from 2024.

The elastic modulus is a measure of a material's stiffness, defined as the ratio of tensile stress to tensile strain. This property is intrinsic to the material and does not directly depend on its density. In the present study, the elastic properties were measured using the impulse excitation of vibration technique. Solid materials have a set of mechanical resonant frequencies (f_r) that are related to their mass, dimensions, and elastic properties. During the measurement process, the sample is impacted using a simple tool that consists of a steel ball glued to the end of a flexible polymer rod. The vibration of the sample is then recorded by a microphone. The so-called resonant frequency and damping analyzer amplifies and processes the transducer signal, which is subsequently used to determine the f_r values through Fourier analysis. If the specimen's shape, dimensions, and mass are known, the elastic moduli are calculated from the f_r values using the relationships outlined in ASTM C 1259–96 [25]. An acoustic device from IMCE nv (Belgium), specifically the Resonant Frequency and Damping Analyser (RFDA) – System 23, was used for this purpose. The dynamic Young's and Coulomb's moduli of the stainless-steel coupons were measured before and after conducting corrosion tests with molten salts. Before the measurements, the oxide layer on the surface of the coupons was removed through a descaling process, as outlined in section C.7.10 of ISO 17245. Additionally, the mass and dimensions of the coupons were accurately determined using METLLER AT 400 FACT balance, which has an accuracy of 1 mg, and a MITUTOYO caliper with a precision of 0.05 mm, respectively.

3. Results and discussion

3.1. Influence of surface preparation

The influence of the surface preparation of AISI 430 ferritic steel samples prior to corrosion testing is presented in Fig. 1, which compares the corrosion rates of polished and unpolished samples over different immersion time. This figure highlights a significant difference in corrosion rate values during the initial times. However, after the initial times, it can be seen that surface preparation does not influence the results of corrosion rate.

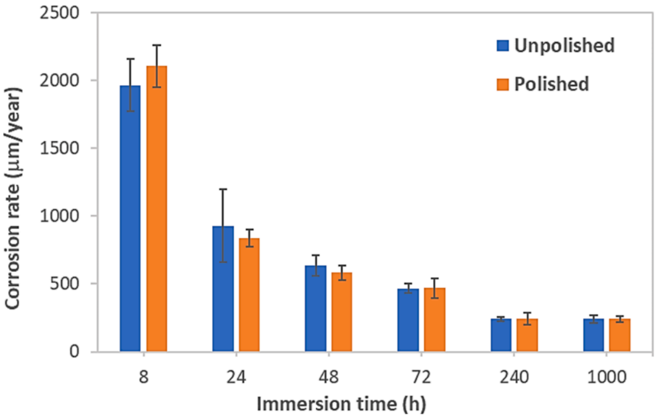

Fig. 1. Corrosion rates of unpolished and polished AISI 430 after exposure to LiNaK carbonate salt at 650 °C for up to 1000 h.

3.2. Selection of descaling process

The changes in mass and images of the corroded AISI 316L austenitic steel samples after each descaling process using three different descaling methods selected are shown in Fig. 2. The results indicate that Method 1 required the fewest descaling steps to achieve a constant mass, and the surface appearance was nearly identical to that of the original steel. In contrast, Method 2 failed to remove the oxide scales, preventing the calculation of the corrosion rate, while Method 3 not only removed the oxides but also resulted in the removal of base material, leading to an increased corrosion rate. Therefore, using unsuitable descaling methods (such as Methods 2 and 3) can lead to inaccurate assessments of corrosion rates. The most effective descaling method for this study is Method 1, outlined in section C.7.10 of the ISO 17245 standard. In conclusion, these results demonstrate that the use of different descaling methods leads to significantly different values in corrosion rates.

Other studies [26,27] have examined how different descaling methods affect the corrosion resistance of various steels exposed to molten salts. These studies highlight the significance of selecting the adequate descaling method in order to accurately evaluate the corrosion rate. The authors stress that choosing the appropriate descaling method is crucial for determining the corrosion rate effectively.

It is important to note that the corrosion rates presented below are based on the results obtained using descaled Method 1, and on samples that were previously polished.

3.3. Specific net mass change kinetics and corrosion rate

The results of the mass gain, mass loss and corrosion rate of the two types of stainless steels immersed in the LiNaK carbonate salt at 650 °C are shown in Fig. 3. Both steels show a similar trend in mass gain and loss, which increased with increasing immersion times (Fig. 3a and b) and the corrosion rate looks like an asymptote (Fig. 3c). In the initial stages of corrosion, both steels undergo an accelerated oxidation process. This phenomenon is attributed to a redox reaction that occurs when the LiNaK carbonate salt comes into direct contact with the steel surface. After a certain period of exposure, the corrosion products formed on the steel surface significantly inhibit further reaction between the molten salt and the steel. This protective layer helps regulate the corrosion reaction rate, leading to a gradual reduction and stabilization of corrosion values after 240 h of immersion in the carbonate salt at 650 °C.

The corrosion rate of AISI 430 is higher than that of AISI 316L. These

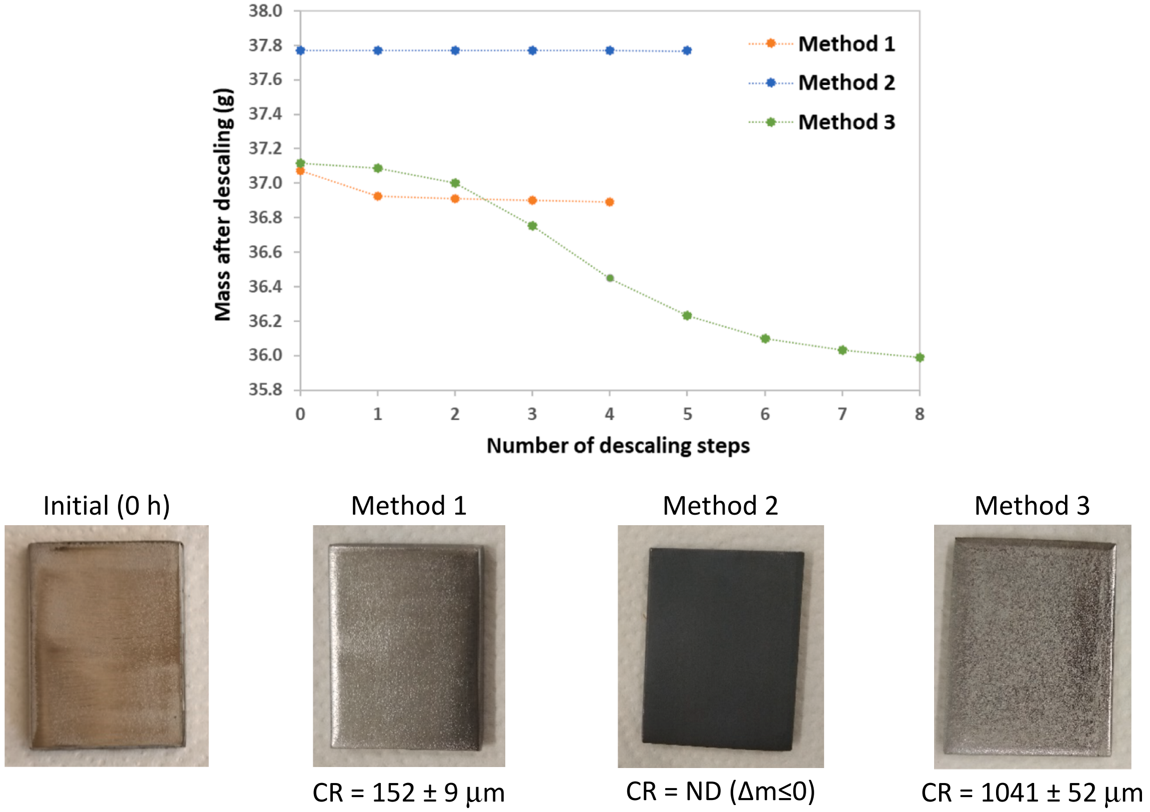

Fig. 2. Results obtained after the three descaling methods (mass after descaling and corrosion rate (CR)) obtained with AISI 316L samples immersed in the LiNaK carbonate salt during 264 h at 650 °C.

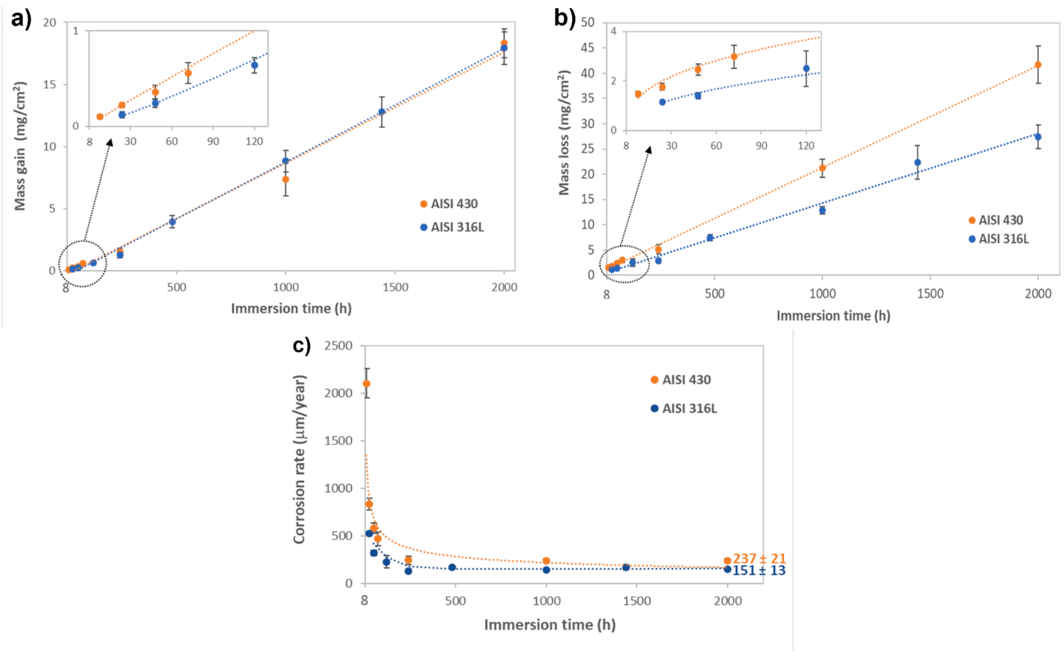

Fig. 3. Mass gain (a), mass loss (b) and corrosion rate (c) of AISI 430 and AISI 316L immersed in the LiNaK carbonate salt up to 2000 h at 650 °C.

differences are particularly pronounced during the early stages of exposure, specifically within the first 240 h. After 2000 h of exposure, the corrosion rate for AISI 430 was 237 ± 21 µm/year while for AISI 316L, it was 151 ± 13 µm/year. The ferritic steels have lower corrosion resistance than austenitic steels, so it was expected that AISI 430 would have higher corrosion values than AISI 316L. Although it is not possible to directly compare the corrosion rates obtained under varying conditions (such as immersion time, temperature, molten salt composition, and the methodologies used for evaluating corrosion rates), the two steels being examined show values that fall within the same order of

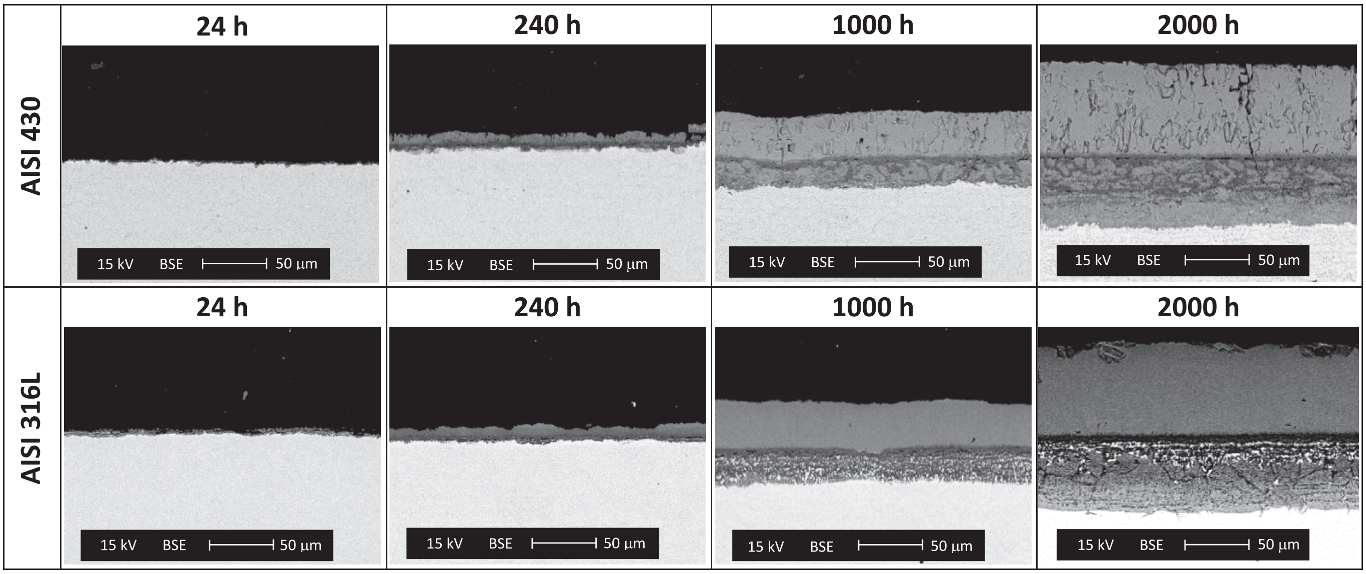

Fig. 4. SEM cross-section images obtained with BSE detector of the oxide scales formed on AISI 430 and AISI 316L after different immersion times in LiNaK carbonate salt at 650 °C (scale bar is 50 µm). The steel substrate is towards the bottom of each image.

magnitude as those listed in Table 1.

3.4. Morphological and chemical characterization of oxide layers and corrosion products

3.4.1. SEM/EDS

Fig. 4 shows cross-sectional images of the oxide layers formed after immersing AISI 430 and AISI 316L steels in LiNaK carbonate salt at 650 °C for 24, 240, 1000, and 2000 h. Distinct layers can be observed, particularly after longer exposure times in both stainless steels. In AISI 430, the first layer (external layer) is less compact than AISI 316L, exhibiting greater porosity and cracking. In contrast, the layer in AISI 316L is more homogeneous.

Fig. 5 and Fig. 6 display the linescans and EDS maps for AISI 430 and AISI 316L steels after 2000 h of exposure in carbonate salt at 650 °C, respectively. Both steels exhibit four distinct oxide sublayers. From the external layer to the substrate, for AISI 430 steel, the first layer shows a higher concentration of Fe and O. The second layer predominantly consists of O and Cr, while the third layer and the fourth layer contain O, Cr and Fe. In the AISI 316L steel, the first layer also shows a higher concentration of Fe and O. The second layer predominantly consists of O and Cr, and the third and fourth layers contain O, Cr, Fe, and Ni.

Fig. 7 highlights the evolution of the total oxide thickness layers over time, based on SEM measurements taken at 15 sample locations. After 2000 h of exposure, the average layer thickness on AISI 430 is 131 ± 5 µm, comprising 59 ± 2 µm from the inner layers (2nd, 3rd, and 4th) and 72 ± 2 µm from the outer layer (1st). In contrast, AISI 316L shows an average layer thickness of 146 ± 10 µm, with 69 ± 7 µm from the inner layers (2nd, 3rd, and 4th) and 77 ± 4 µm from the outer layer (1st).

The results indicate a linear and continuous increase in the total layer thickness over time, which is in good agreement with the observed mass losses, due to uniform corrosion. In other words, the base metal is subject to gradual corrosion over time, resulting in an incremental accumulation of oxide layers. Thus, the loss of mass is a consequence of the formation of these oxides, which are subsequently removed during the descaling process. However, the steel with the highest rate has the lowest thickness. This phenomenon can be attributed to the reduced cohesion and increased brittleness of the oxides formed on ferritic steel, as evidenced by the SEM images (Figs. 4 and 5), which reveal the presence of pores and cracks in the layer. In contrast to the more compact layer of austenitic steel, which is characterized by the presence of nickel, an element known to stabilize the oxides formed.

3.4.2. Metallography

The microstructures of both the reference samples and the samples immersed in the carbonate salt for 2000 h are shown in Fig. 8. The base metal of the AISI 430 steel consists of ferrite grains [28–30]. After being exposed to the carbonate salt at 650 °C for 2000 h, it was observed that the grain size near the oxide layer has increased. Additionally, chromium carbide precipitates are present at the grain boundaries, as visualized by SEM/EDS analysis.

In the case of AISI 316L, it was observed that the base metal contained austenitic polygonal grains [28,29], as well as annealing twins formed during the rolling process of this steel. After 2000 h of exposure, the grains became finer near the oxide layer, and the grain boundaries exhibited chromium carbide precipitates. Furthermore, deformation twins were also formed in this steel. As illustrated in Fig. 7, the oxide thickness indicates that the depth of affectation seems to be greater in austenitic compared to ferritic steel, which supports the consistency of the findings. However, these results do not provide sufficient evidence to conclude that AISI 430 reveal a higher susceptibility to corrosion when compared to AISI 316L.

3.4.3. GDOES

Because Li has a low atomic number, it cannot be detected using EDS analysis. Therefore, it was necessary to use a complementary characterization technique, namely GDOES. This tool can efficiently and quickly track the depth distribution of both light and heavy elements, allowing the evaluation of lithium distribution within the various oxide sublayers formed.

Fig. 9 shows the composition profiles of specimens that were exposed to LiNaK carbonates for 24 and 1000 h at 650 °C, as measured by GDOES. The x-axis (time) is proportional to the thickness of the oxide layer formed on the surface of the substrate. An analysis of the profiles indicates that lithium is present throughout the oxide layers formed.

In both types of steels, after 24 h of exposure, the distribution of the elements present is similar. Specifically, the profiles of O and Mg decreased in intensity as they approached the substrate, eventually disappearing entirely. The intensity of Fe in the oxide layer remained constant; however, there was a notable increase in intensity at the interface with the substrate. In contrast, the intensities of Li and Cr increased throughout the oxide layer and then decreased beyond the

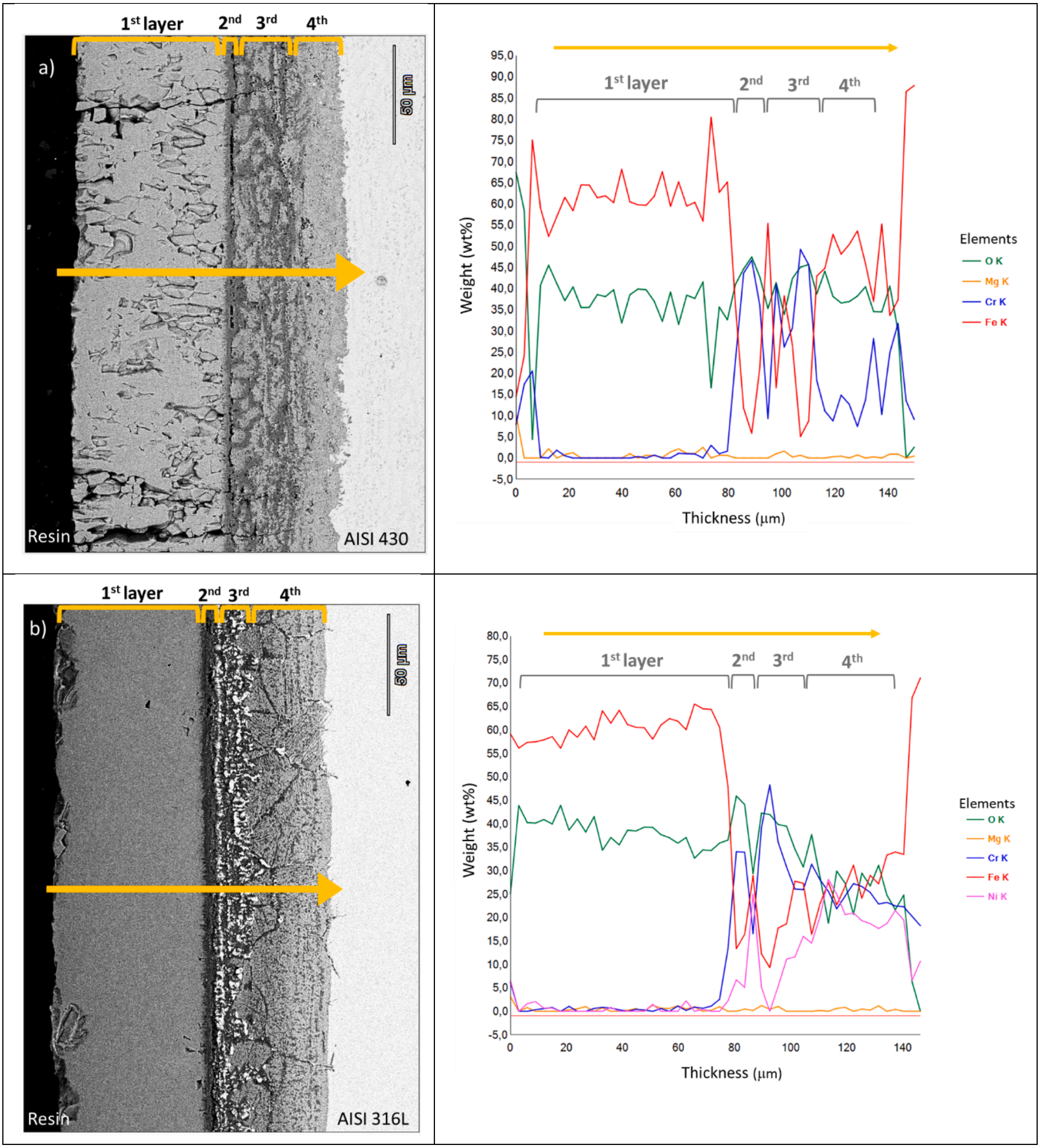

Fig. 5. Cross-sectional linescans of SEM micrographs obtained after 2000 h of immersion in carbonate salt at 650 °C. The corresponding elemental chemical composition was obtained by EDS of two different types of steel: a) AISI 430 and b) AISI 316L.

point of substrate detection. In the case of austenitic steel, Ni is also present, although it mainly exists in the substrate. Thus, it can be concluded that an oxide layer was formed, consisting of both lithium–iron oxides and lithium-chromium oxides.

At 1000 h of exposure, the profiles of the various elements showed distinct differences in intensity, indicating the evolving composition of the layers under analysis. The oxygen profile exhibited consistent intensity before the substrate. The intensity of Fe was higher in the superficial layer but decreased as the intensity of Cr increased, creating a balance between the intensities of these two elements in the surface layer. Following the detection of the substrate, the intensity of Fe increased again. Regarding Li, this element displayed the highest intensity throughout the oxide layer, with the greatest intensity found in the layers adjacent to the substrate, after which its intensity decreased drastically. It is also noteworthy that in AISI 316L, Ni is present only in the layers closest to the substrate. It can thus be concluded that the

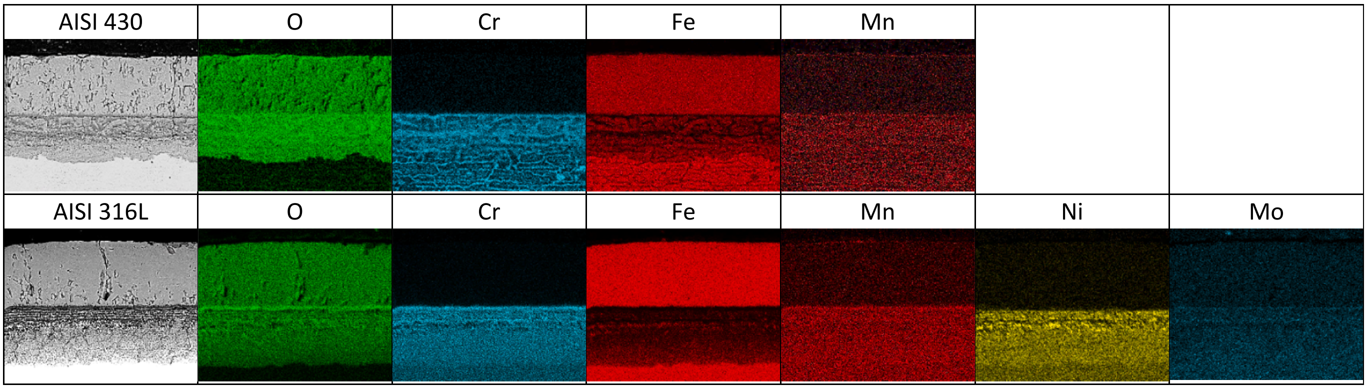

Fig. 6. Backscattered electrons image and corresponding EDS maps for the AISI 430 and AISI 316L samples after LiNaK carbonate salt exposure for 2000 h at 650 °C (Scale bar is 50 µm).

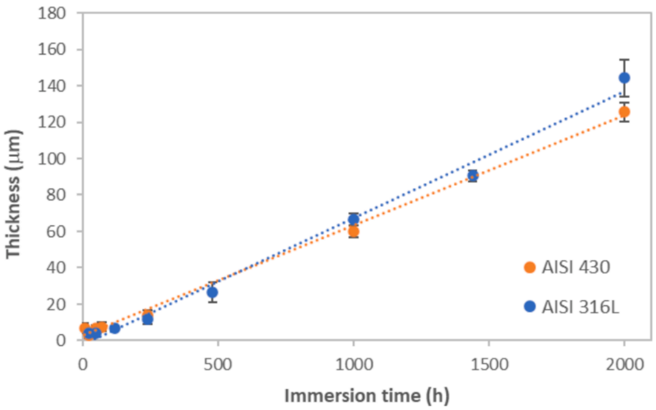

Fig. 7. Evolution of the thickness of the oxide layers of the AISI 430 and AISI 316L samples after LiNaK carbonate salt exposure for 2000 h at 650 °C.

external layer is predominantly composed of oxygen, iron, and lithium, while the internal layers closer to the substrate, also contain chromium and nickel in the case of AISI 316L steel.

The findings from this technique are in agreement with those of other techniques, namely regarding the formation of oxides in a multilayer structure.

3.4.4. XRD

Fig. 10 presents the X-ray diffraction patterns of both steels after exposure for 24, 240, 1000, and 2000 h. Generally, the diffraction patterns of the two steels were similar, except for AISI 316L, which shows the presence of nickel oxide (NiO). This is attributed to nickel being one of the primary components of austenitic steel, unlike ferritic steel. As a result, both steels exhibited similar oxide formation. The analysis of the pattern at 24 h revealed the formation of lithium chromium ($LiCrO_2$) and lithium iron ($LiFeO_2$ and $Li_5Fe_5O_8$) spinels, along with MgO. Magnesium is an element present as an impurity in salts. Other authors have also detected magnesium oxides in the surface layer [10,12]. From 240 h to 2000 h, the patterns show a high degree of similarity, indicating that the corrosion products during this period consist mainly of $Li_5Fe_5O_8$ and MgO. Notably, the increasing intensity of the $Li_5Fe_5O_8$ peaks over time confirms that this compound is present in the outermost layer, with its concentration increasing as time progresses. The XRD results support the findings from the SEM analysis, which also indicated the presence of chromium and nickel oxides after shorter exposure times and at the first sublayers. As exposure time increased, iron became more prevalent, resulting in the formation of $LiFeO_2$ and $Li_5Fe_5O_8$ in the external layers.

3.4.5. Dynamic elastic moduli

The effect of immersion time on both the Young's and Coulomb's modulus of the corroded coupons is shown in Fig. 11. It was observed that AISI 316L steel is less stiff compared to AISI 430 steel.

Both types of stainless-steel exhibit no significant differences in their elastic moduli after 2000 h of exposure. However, a slight downward trend is observed in AISI 430 up to 1000 h. Indeed, it is noteworthy that corrosion degradation can influence the elastic properties of steels [31]. The phenomenon of intergranular corrosion occurred in both steels and may be responsible for these small differences.

When examining the observed E values, the Young's modulus of AISI 316L steel (~205 GPa) falls within the expected range. In contrast, the Young's modulus of AISI 430 steel was about 16 % higher than that of AISI 316L, reaching around 235 GPa [32,33]. Unlike the elastic properties measured in tensile tests, dynamic values determined from resonant frequencies depend on the mass and dimensions of the samples. Consequently, the measured elastic moduli values may have been affected by several factors, including dimensional variability, surface finish, edge conditions, and the fact that the samples had not been rectified prior to measurement. These factors likely contributed to a decrease in measurement precision, potentially impacting the determined values.

As already pointed out, it was noted that the standard deviation of the E values measured for the samples after 2000 h of exposure showed an unexpected increase. This increase was attributed to the extensive corrosion observed, which resulted in a more irregular surface once the oxides were removed. Consequently, this irregularity led to discrepancies in the measurements of the dimensions across different samples, helping to explain the observed change in trend. It is well known that the results of dynamic modulus tests are influenced by both external factors (such as surface roughness and geometric irregularities) and internal factors (including porosity and cracks) in the samples [34].

The same trend was seen with Coulomb's modulus (Fig. 11b). Another important parameter to consider is Poisson's ratio (ν). Young's modulus and shear modulus are related by $E = 2G(1 + \nu)$, for isotropic and homogeneous materials. Both stainless steels exhibit a ν value of 0.27, which is in good agreement with data reported elsewhere [32]. This suggests that both steels exhibit a high degree of isotropy.

The core stiffness of stainless steels appears unaffected by exposure to molten salt or high temperatures, based on data collected after 2000 h of exposure.

3.4.6. Corrosion mechanism

The reaction involved in the decomposition of the ternary salt based on LiNaK carbonates produces carbon dioxide (CO_2) and results in the formation of an alkali metal oxide (A_2O). This reaction can be expressed as follows:

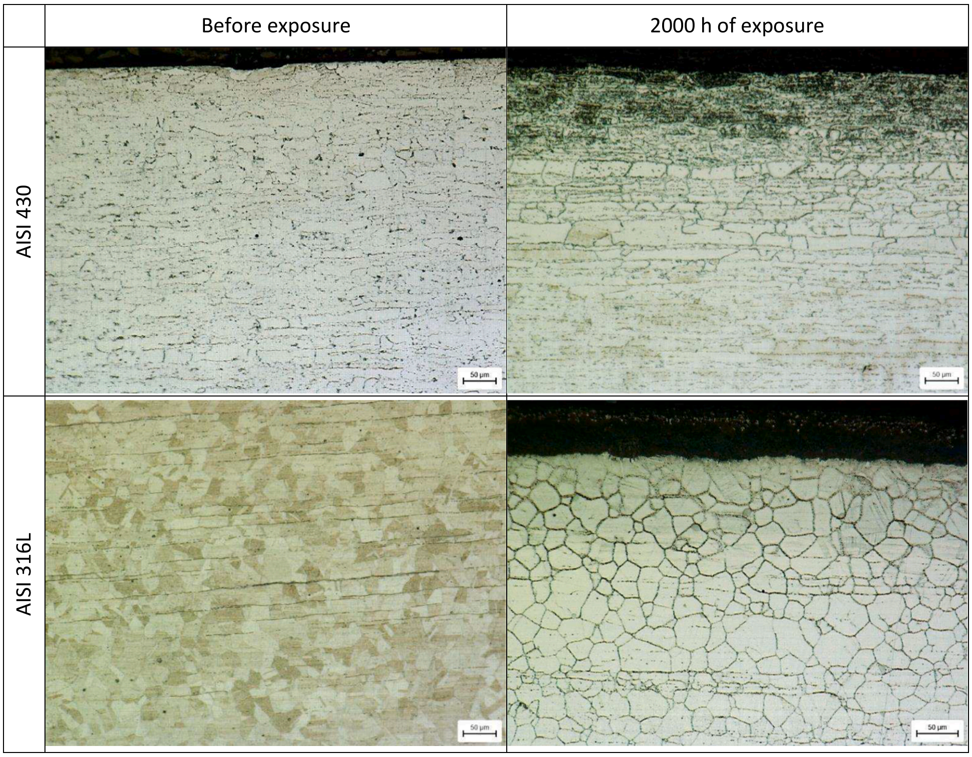

Fig. 8. Microstructures of AISI 430 and AISI 316L steels before and after 2000 h of exposure to molten carbonate salts at 650 °C.

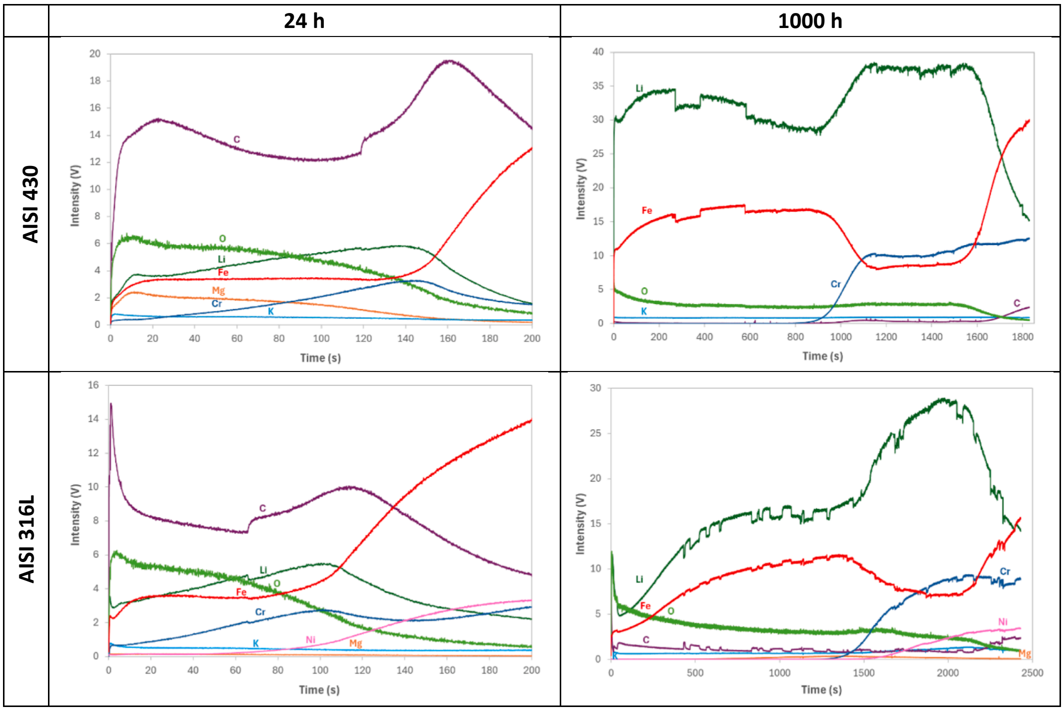

Fig. 9. GDOES depth profiles of elements after exposure of both steels at 650 °C in carbonate LiNaK salt for 24 h and 1000 h.

$$A_2CO_3 \rightleftharpoons A_2O + CO_2 \quad (2)$$

where A represents the element Li, Na and K.

XRD analysis has shown that Li is the alkali metal that forms oxides most readily. This observation is in agreement with the findings of Luo et al. [8], which indicates that the activity of Li_2O is higher than that of K_2O and Na_2O. They noticed that Li_2O completely dissociates into Li^+ and O^{2-} ions in the molten salt. Furthermore, De Miguel *et al.* [35] have reported that lithium carbonate's basicity is higher than that of sodium and potassium carbonates. As a result, lithium oxides are preferentially formed. Luo *et al.* [8] also emphasized that the chromium present in stainless steel is more susceptible to oxidation than other alloying elements, due to its greater affinity for oxygen from a thermodynamic viewpoint.

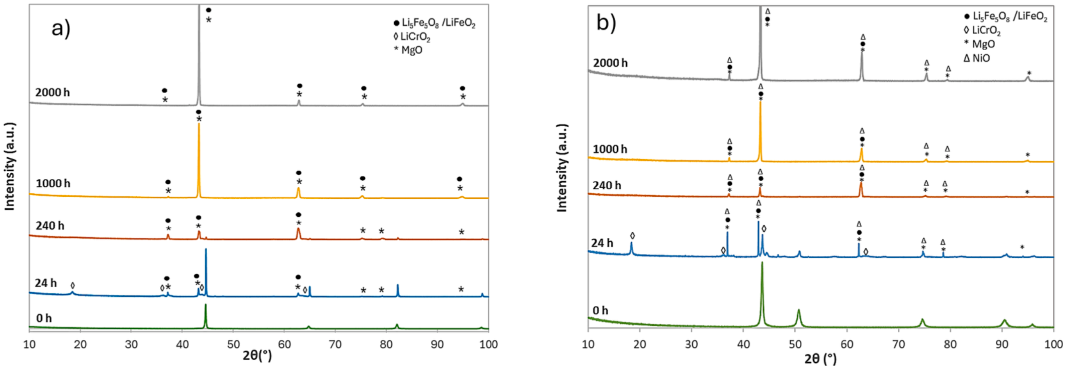

Fig. 10. XRD patterns of AISI 430 (a) and AISI 316L (b) after exposure in LiNaK carbonate salt for different times, at 650 °C.

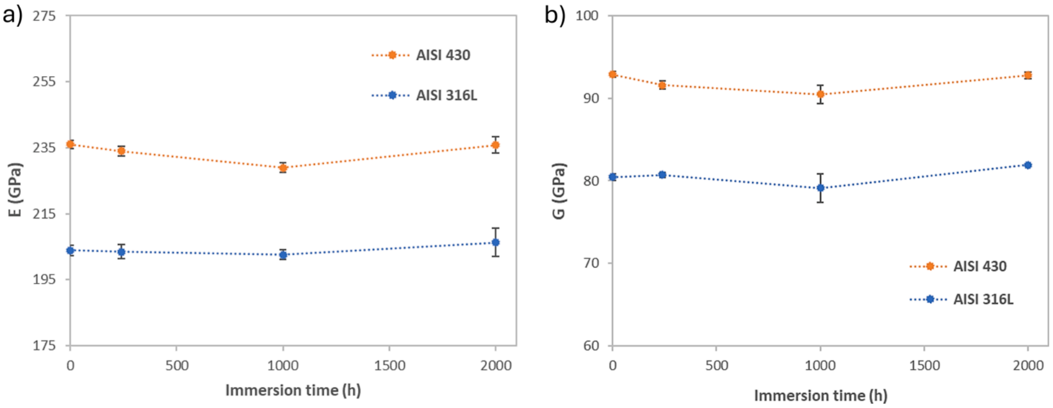

Fig. 11. Young’s modulus (a) and Coulomb’s modulus (b) dependence on immersion time for two stainless steels AISI 430 and AISI 316L after exposure at 650 °C.

As a result of chromium migrating to the surface, lithium’s high activity and basicity cause chromium to preferentially bind to Li^+. Only then does the Fe-Li oxide form, as indicated by the possible equations below:

$$Cr_2O_3 + O^{2-} + 2Li^+ \rightleftharpoons 2LiCrO_2 \tag{3}$$

$$Fe_2O_3 + O_2 + 2Li^+ \rightleftharpoons 2LiFeO_2 \tag{4}$$

$$Fe^{3+} + Li^+ + 2O_2 \rightleftharpoons LiFeO_2 \tag{5}$$

$$5/2Fe_2O_3 + 1/2O^{2-} + 5Li^+ \rightleftharpoons Li_5Fe_5O_8 \tag{6}$$

$$LiFeO_2 + 6O_2 + 4Fe^{3+} + 4Li^+ \rightleftharpoons Li_5Fe_5O_8 \tag{7}$$

The proposed sequence of reactions is based on the results obtained from the XRD analysis, where the compounds indicated were identified. Neither K- nor Na- containing reaction products were detected.

The formation of NiO, as noted in Eq. (8), was observed in the corrosion tests on AISI 316L steel thereby enhancing the protective character of the surface layer, effectively reducing the corrosion rate. This is in line with findings reported by other authors [35].

$$\mathrm{Ni} + \mathrm{CO}_3^{2-} = \mathrm{NiO} + \mathrm{CO}_2 + 2\mathrm{e}^- \tag{8}$$

As the exposure time increased, outward diffusion of Fe^{3+} ions through the existing oxides on the surface of the sample, enabled the growth of the $Li_5Fe_5O_8$ layer.

As the thickness of the $Li_5Fe_5O_8$ layer continued to grow with prolonged exposure, there came a point where it became challenging to detect the $LiCrO_2$ layer beneath it by XRD. This is why the $LiCrO_2$ phase is absent from the diffractograms of the longer exposure times, as shown in Fig. 10.

The presence of impurities in molten salts can also result in the formation of oxides, such as magnesium, which forms MgO. In this study, no iron or chromium spinel was observed, contrasting with the findings of other studies [6,10,12].

Additionally, the corrosion products were observed to form a multilayer structure, in accordance with findings from other studies [8,27,35,36].

Fig. 12 illustrates a schematic of the overall oxide layers that were formed on the surface of each steel. It displays the various oxides present within each sub-layer, which have been identified through a combination of SEM-EDS, GDOES, and XRD analyses.

4. Conclusions

This study compares the corrosion rates and mechanism of ferritic steel (AISI 430) and austenitic steel (AISI 316L) when in contact with a ternary mixture of LiNaK carbonates at 650 °C, for up to 2000 h. Corrosion rates differ significantly during the early stage which diminish over time, with AISI 430 reaching 237 ± 21 μm/year and AISI 316L at 151 ± 13 μm/year, after 2000 h.

The results of this study, when compared with existing literature, highlight the importance of standardizing the methodologies used. In particular, longer immersion times are necessary to achieve stabilization of the corrosion rate, and effective descaling methods must be employed to remove oxides without damaging the base metal. Maintaining consistent conditions is crucial for accurately comparing the corrosion rates of different steels.

Morphological and chemical analysis reveal that a multilayer corrosion structure is formed in both steels, with a total thickness of 131 ± 5 μm (AISI 430) and 146 ± 10 μm (AISI 316L). The corrosion products that formed in the initial layers (those closest to the substrate) were

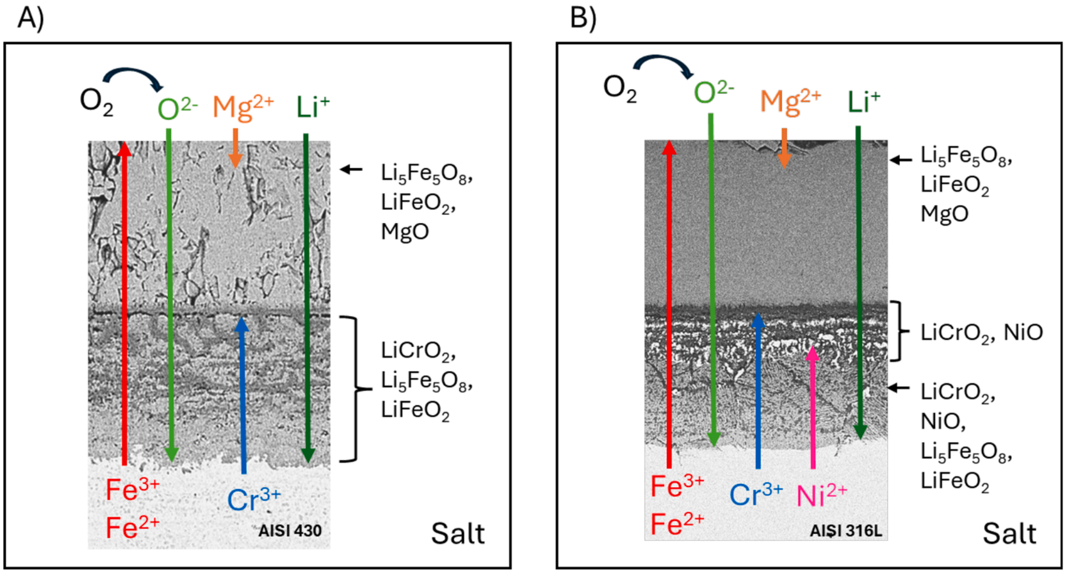

Fig. 12. Schematic corrosion mechanism of (a) AISI 430 and (b) AISI 316L steels after 2000 h immersion in LiNaK ternary salt at 650 °C.

$LiCrO_2$ and $Li_5Fe_5O_8$/$LiFeO_2$ for both steels, and additionally NiO for AISI 316L. On the surface, the corrosion products were $Li_5Fe_5O_8$/$LiFeO_2$ and MgO.

The metallographic tests demonstrated that both steels are sensitized due to oxide layers formed and chromium carbide precipitates, but core stiffness seems unaffected by exposure to molten LiNaK salt at 650 °C.

Although AISI 430 steel has a higher corrosion rate than AISI 316L, the structural differences are not very significant when exposed to LiNaK molten salt for up to 2000 h. However, the corrosion rate for both cases exceeds the specified limit of 20 μm/year, which is required for a CSP plant intended to operate for 30 years [37]. To overcome this problem, the search for alternative materials resistant to molten salt corrosion, such as nickel alloys and other superalloys, is the first thought of solution, but the high cost limits their widespread use in CSP systems. On the other hand, considering the low cost, structural stability and corrosion resistance of AISI 430, it can be a viable alternative if used with an appropriate coating to prevent corrosion.

Funding

The funding provided by FCT – Fundação para a Ciência e a Tecnologia, I.P. through national funds for the project NEWS4CSP is acknowledged (https://doi.org/10.54499/2022.05021.PTDC).

CRediT authorship contribution statement

Mafalda Gil: Methodology, Formal analysis, Writing – original draft, Data curation, Investigation. **Fátima Pedrosa:** Writing – review & editing, Investigation, Methodology, Data curation. **Teresa Paiva:** Formal analysis. **Isabel Figueira:** Formal analysis. **Fernando A. Costa Oliveira:** Investigation, Validation, Writing – review & editing, Formal analysis. **Teresa C. Diamantino:** Project administration, Conceptualization, Supervision, Data curation, Writing – review & editing, Investigation.

References

[1] A.H. Alami, A.G. Olabi, A. Mdallal, A. Rezk, A. Radwan, S.M.A. Rahman, S.K. Shah, M.A. Abdelkareem, Concentrating solar power (CSP) technologies: Status and analysis, Int. J. Thermofluids. 18 (2023) 100340, https://doi.org/10.1016/j.ijft.2023.100340.

[2] M. Walczak, F. Pineda, Á.G. Fernández, C. Mata-Torres, R.A. Escobar, Materials corrosion for thermal energy storage systems in concentrated solar power plants, Renew. Sustain. Energy Rev. 86 (2018) 22–44, https://doi.org/10.1016/j.rser.2018.01.010.

[3] I. Arias, E. Zarza, L. Valenzuela, M. Pérez-García, J.A. Romero Ramos, R. Escobar, Modeling and hourly time-scale characterization of the main energy parameters of parabolic-trough solar thermal power plants using a simplified quasi-dynamic model, Energies 14 (1) (2021) 221, https://doi.org/10.3390/en14010221.

[4] P. Kondaiah, R. Pitchumani, Progress and opportunities in corrosion mitigation in heat transfer fluids for next-generation concentrating solar power, Renew. Energy 205 (2023) 956–991, https://doi.org/10.1016/j.renene.2023.01.044.

[5] A. Caraballo, S. Galán-Casado, Á. Caballero, S. Serena, Molten Salts for Sensible thermal Energy Storage: a Review and an Energy Performance Analysis, Energies 14 (4) (2021) 1197, https://doi.org/10.3390/en14041197.

[6] A.G. Fernández, L.F. Cabeza, Corrosion monitoring and mitigation techniques on advanced thermal energy storage materials for CSP plants, Sol. Energy Mater. Sol. Cells 192 (2019) 179–187, https://doi.org/10.1016/j.solmat.2018.12.028.

[7] V.M.B. Nunes, M.J.V. Lourenço, F.J.V. Santos, C.A. Nieto de Castro, Molten alkali carbonates as alternative engineering fluids for high temperature applications, Appl. Energy 242 (2019) 1626–1633, https://doi.org/10.1016/j.apenergy.2019.03.190.

[8] J. Luo, C.K. Deng, N. Tariq, H. ul, N. Li, R.F. Han, H.H. Liu, J.Q. Wang, X.Y. Cui, T. Y. Xiong, Corrosion behavior of SS316L in ternary Li2CO3–Na2CO3–K2CO3 eutectic mixture salt for concentrated solar power plants, Sol. Energy Mater. Sol. Cells 217 (2020) 110679, https://doi.org/10.1016/j.solmat.2020.110679.

[9] V. Encinas-Sánchez, M.T. de Miguel, G. García-Martín, M.I. Lasanta, F.J. Pérez, Corrosion resistance of Cr/Ni alloy to a molten carbonate salt at various temperatures for the next generation high-temperature CSP plants, Sol. Energy 171 (2018) 286–292, https://doi.org/10.1016/j.solener.2018.06.091.

[10] L. Ma, C. Zhang, Y. Wu, Y. Lu, Comparative review of different influence factors on molten salt corrosion characteristics for thermal energy storage, Sol. Energy Mater. Sol. Cells 235 (2022) 111485, https://doi.org/10.1016/j.solmat.2021.111485.

[11] F. Sutter, C. Oskay, M.C. Galetz, T. Diamantino, F. Pedrosa, I. Figueira, S. Glumm, A. Bonk, A. Agüero, S. Rodríguez, et al., Dynamic corrosion testing of metals in solar salt for concentrated solar power, Sol. Energy Mater. Sol. Cells 232 (2021) 111331, https://doi.org/10.1016/j.solmat.2021.111331.

[12] A. Gomes, M. Navas, N. Uranga, T. Paiva, I. Figueira, T.C. Diamantino, High-temperature corrosion performance of austenitic stainless steels type AISI 316L and AISI 321H, in molten Solar Salt, Sol. Energy 177 (2019) 408–419, https://doi.org/10.1016/j.solener.2018.11.019.

[13] M. Tavakoli, M. Gholami-Kermanshahi, V.W.M. Neubert, Effects of molten-salt LiNO3 on high-temperature corrosion behaviour of absorption tubes of a concentrating solar power system, Corros. Eng. 55 (2020) 18–26, https://doi.org/10.1080/1478422X.2019.1663027.

[14] V. Encinas-Sánchez, E. Batuecas, A. Macías-García, C. Mayo, R. Díaz, F.J. Pérez, Corrosion resistance of protective coatings against molten nitrate salts for thermal energy storage and their environmental impact in CSP technology, Sol. Energy 176 (2018) 688–697, https://doi.org/10.1016/j.solener.2018.10.083.

[15] J. Gallardo-González, M. Martínez, C. Barreneche, A.I. Fernández, M. Liu, N.H. S. Tay, F. Bruno, M. Segarra, Corrosion of AISI316 as containment material for latent heat thermal energy storage systems based on carbonates, Sol. Energy Mater. Sol. Cells 186 (2018) 1–8, https://doi.org/10.1016/j.solmat.2018.06.003.

[16] T. Liu, X. Xu, W. Liu, X. Zhuang, Corrosion of alloys in high temperature molten-salt heat transfer fluids with air as the cover gas, Sol. Energy 191 (2019) 435–448, https://doi.org/10.1016/j.solener.2019.09.015.

[17] P. Audigié, V. Encinas-Sánchez, S. Rodríguez, F.J. Pérez, A. Agüero, High temperature corrosion beneath carbonate melts of aluminide coatings for CSP

application, Sol. Energy Mater. Sol. Cells 210 (2020) 110514, https://doi.org/10.1016/j.solmat.2020.110514.

[18] L. González-Fernández, A. Anagnostopoulos, T. Karkantonis, O. Bondarchuk, S. Dimov, M. Chorążewski, Y. Ding, Y. Grosu, Laser-induced carbonization of stainless steel as a corrosion mitigation strategy for high-temperature molten salts applications, J. Storage Mater. 56 (2022) 105972, https://doi.org/10.1016/j.est.2022.105972.

[19] S.P. Sah, Evolution of corrosion resistance of 310S stainless steel in carbonates melt at 650 °C, Corros. Sci. 226 (2024) 111663 https://doi.org/10.1016/j.corsci.2023.111663.

[20] M. Morales, M. Rezayat, G. Fargas, A. Mateo, Mitigating the corrosion of AISI 301LN steel in molten carbonate salts by doping with alumina nanoparticles for thermal energy storage applications, Sol. Energy Mater. Sol. Cells 270 (2024) 112805, https://doi.org/10.1016/j.solmat.2024.112805.

[21] M. Morales, M. Rezayat, A. Mateo, Enhancing the corrosion resistance of 2205 duplex stainless steel in molten carbonate salts by laser-surface texturing, J. Storage Mater. 78 (2024) 110053, https://doi.org/10.1016/j.est.2023.110053.

[22] R.I. Olivares, C. Chen, S. Wright, The thermal Stability of Molten Lithium–Sodium–Potassium Carbonate and the Influence of Additives on the Melting Point, J. Sol. Energy Eng. 134 (4) (2012) 041002, https://doi.org/10.1115/1.4006895.

[23] ISO 17245:2015 - Corrosion of metals and alloys — Test method for high temperature corrosion testing of metallic materials by immersing in molten salt or other liquids under static conditions. 2015.

[24] ISO 8407:2021 - Corrosion of metals and alloys — Removal of corrosion products from corrosion test specimens. 2021.

[25] ASTM C1259-94 - Standard Test Method for Dynamic Young's Modulus, Shear Modulus, and Poisson's Ratio for Advanced Ceramics by Impulse Excitation of Vibration. 1994.

[26] T. Diamantino, M. Navas, E. Veca, F. Pedrosa, Dynamic corrosion methodologies of molten salts. Deliverable 6.1 of the project Sfera III – Solar Facilities for the European Research, Area (2023).

[27] P. Audigié, S. Rodríguez, A. Agüero, F. Pedrosa, T. Paiva, T.C. Diamantino, Comparison of descaling methods to study the corrosion kinetics of ferritic steels after dynamic exposure to molten carbonates, Corros. Sci. 209 (2022) 110786, https://doi.org/10.1016/j.corsci.2022.110786.

[28] ASM Handbook Committee. Metals Handbook. 8th ed. 1972.

[29] ASM Handbook Committee. Metals Handbook. 9th ed. 1985.

[30] M. POURANVARI, S. P. H. MARASHI, M. ALIZADEH-SH. Welding metallurgy of dissimilar AISI 430/DQSK steels resistance spot welds. 2015.

[31] Z. Chen, S. Nie, W. Han, M. Tang, B. Yang, M. Elchalakani, A study on static properties of high-performance steel after corrosion damage, J. Constr. Steel Res. 207 (2023) 107970, https://doi.org/10.1016/j.jcsr.2023.107970.

[32] ASM International. ASM Handbook - Properties and Selection: Irons, Steels, and High-Performance Alloys. 1990.

[33] M.F. Slim, A. Alhussein, A. Billard, F. Sanchette, M. François, On the determination of Young's modulus of thin films with impulse excitation technique, J. Mater. Res. 32 (3) (2017) 497–511, https://doi.org/10.1557/jmr.2016.442.

[34] M. Richetta, A. Varone, A Focus on Dynamic Modulus: Effects of External and Internal Morphological Features, Metals 11 (1) (2020) 40, https://doi.org/10.3390/met11010040.

[35] M.T. de Miguel, V. Encinas-Sánchez, M.I. Lasanta, G. García-Martín, F.J. Pérez, Corrosion resistance of HR3C to a carbonate molten salt for energy storage applications in CSP plants, Sol. Energy Mater. Sol. Cells 157 (2016) 966–972, https://doi.org/10.1016/j.solmat.2016.08.014.

[36] L. González-Fernández, M. Intxaurtieta-Carcedo, O. Bondarchuk, Y. Grosu, Effect of dynamic conditions on high-temperature corrosion of ternary carbonate salt for thermal energy storage applications, Sol. Energy Mater. Sol. Cells 240 (2022) 111666, https://doi.org/10.1016/j.solmat.2022.111666.

[37] Luisa F. Cabeza. Advances in Thermal Energy Storage Systems: Methods and Applications. 2^{a} edition. Elsevier; 2020. https://doi.org/10.1016/B978-0-12-819885-8.00030-9.